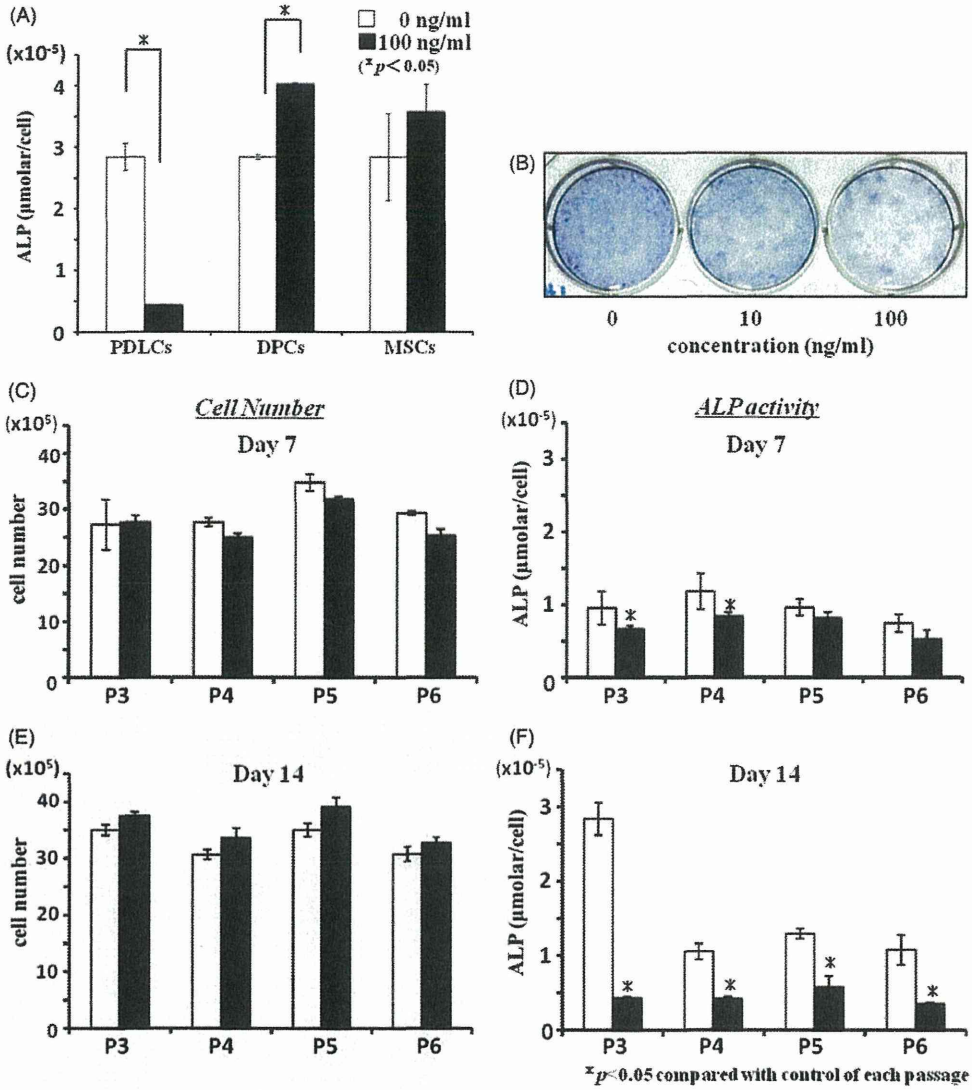

Figure 2. Effects of rmGDF-5 on different cell types. (A) Alkaline phosphatase (ALP) activity on P3 PDLCs, dental pulp-derived cells (DPCs) and mesenchymal stem cells (MSCs) at 14 d of culture. ALP activity in PDLCs decreased significantly by a treatment of 100 ng/ml GDF-5 (*$p < 0.05$). In contrast, ALP activities of P3 DPCs and MSCs were increased by GDF-5 treatment with a statistically significant difference in DPCs. (B) GDF-5 treatment resulted in a reduced ALP staining of cultured PDLCs in a dose-dependent manner. (C, E) Total cell numbers for P3-6 PDLCs at 7 and 14 d of culture. Total cell number did not show a significant difference across all concentrations and passages. (D, F) ALP activities for P3-6 PDLCs at 7 and 14 d of culture. GDF-5 inhibited ALP activity for all passages between P3-6 PDLCs at both day 7 and 14. Most significant differences are shown on day 14 (particularly on P3 cells).

GDF-5 increased the expression of tenomodulin, a mature tenocyte marker, markedly at 21 d (Figure 4D). In contrast, no significant differences were observed for the expressions of *runx2* (a transcription factor of osteogenic differentiation), *sox9* (a transcription factor of chondrogenic differentiation) and *pparγ* (a transcription factor of adipogenic differentiation) (Figure 4E–G).

Discussion

This study demonstrated that exogenous GDFs could reliably enhance the tenogenic/ligamental characteristics of primary cultured human PDLCs. Our outcomes were: (1) recombinant GDF-5 (and/or -7) maintained an inhibitory effect to ALP activity in PDLCs during several passages in culture, and (2) GDF-5 induced high expressions of both early and mature tenogenic genes in PDLCs cultured at late passages, while not enhancing the expressions of specific transcription-factors for osteogenic, chondrogenic and adipogenic differentiations.

Regarding the first outcome, we demonstrated that recombinant GDF-5 and -7 inhibited ALP activity reliably in cultured PDLCs. Our results may be consistent with Nakamura et al. (2003) who demonstrated that GDF-5 stimulated cell proliferation and glycosaminoglycan synthesis, but inhibited ALP activity in cultured PDLCs. However, a detailed characterization of changes in PDLCs treated with GDFs has not been reported. Thus our study confirmed that this inhibitory effect was persistent from passage 3 to 6. During the culture process, we observed that PDLCs had a tendency to down-regulate their osteogenic and tenogenic characteristics (Itaya et al., 2009). In fact, our data showed that the ALP activity of PDLCs after passage 4 was remarkably decreased when compared with that

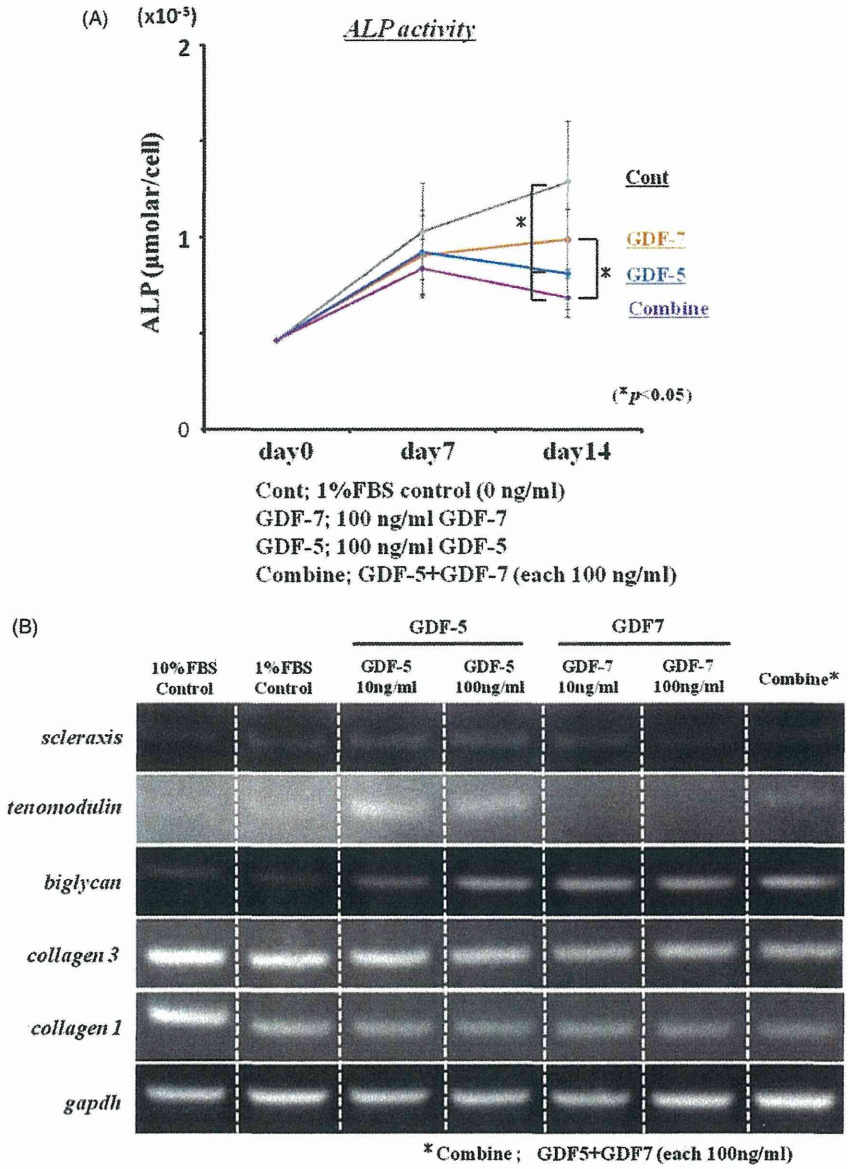

Figure 3. Effects of rmGDF-5 and rhGDF-7 on ALP activity and tenogenic gene expressions. (A) Effects of 100 ng/ml GDF-5 and/or GDF-7 treatments on the ALP activity of P4 PDLCs. GDF-7 reduced ALP activity as compared with non-treatment, but its inhibitory effect was less than that of GDF-5 at 14 d of culture. Combination of both GDFs resulted in the lowest level of ALP activity after 14 d of culture. (B) Changes of tenogenic gene expressions in P4 PDLCs by treatments with GDFs for 7 d in culture. RT-PCR products corresponding to *scleraxis*, *tenomodulin*, *biglycan*, *collagen 3* and *collagen 1* mRNAs. *Gapdh* was used as a loading control.

of cells at passage 3 (Figure 2F). Therefore, the inhibitory effect of GDF-5, alone, at P3 was significant because if these PDLCs P3 cells were not treated with GDF-5, their ALP activities would have remained high (i.e. a high ability of osteoblastic differentiation). GDF-5 was capable to suppress ALP activity to the same levels as that of PDLCs at passage 4–6 (Figure 2F). Moreover, we found recombinant GDF-7 has also an inhibitory effect on ALP activity of PDLCs although its effect was less than that of GDF-5, and that of both GDFs combined. Although the exact role/mechanism of GDFs during periodontal ligament formation has not been described, there are reports that GDFs were expressed in cells within the developing periodontal ligament (Morotome et al., 1998; Sena et al., 2003). And, this finding suggests GDFs to be involved in the formation of the dental-to-bone insertion/attachment apparatus. GDF-5 and -7 might play vital roles in inhibiting calcifications at insertion sites (borders) between bone/cementum and PDL.

In contrast to the inhibitory effect on ALP activity of PDLCs, GDF-5 had enhancing effects on DPCs or MSCs, interestingly. Similarly, we have previously shown that GDF-5 significantly reduced ALP activity in dental follicle-derived cells, while it significantly increased this activity in dental papilla-derived cells (Sumita et al., 2010). These observed differential effects of GDF-5 could depend on the cell types and their specific differentiation fates. GDF-5 promoted ALP activity in the osteo/odontogenic cells such as MSCs, DPCs or dental papilla-derived cells, while inhibited ALP activity in the tenogenic/ligamental cells such as PDLCs or dental follicle-derived cells. In particular, DPCs are believed to be more mature progenitors of osteo/odontoblastic cells. From these results, we speculate that the differential effects of GDF-5 on these cell types might be essential for the final development into bone/dentin or PDL. Therefore, the inhibitory effect of ALP activity displayed by GDFs might be extremely favorable to enhance or to induce the tenogenic characteristics of PDLCs.

With regard to the reliability of enhancing tenocytic induction in cultured PDLCs, our results indicated that GDF-5 strongly induced the expressions of both early and mature

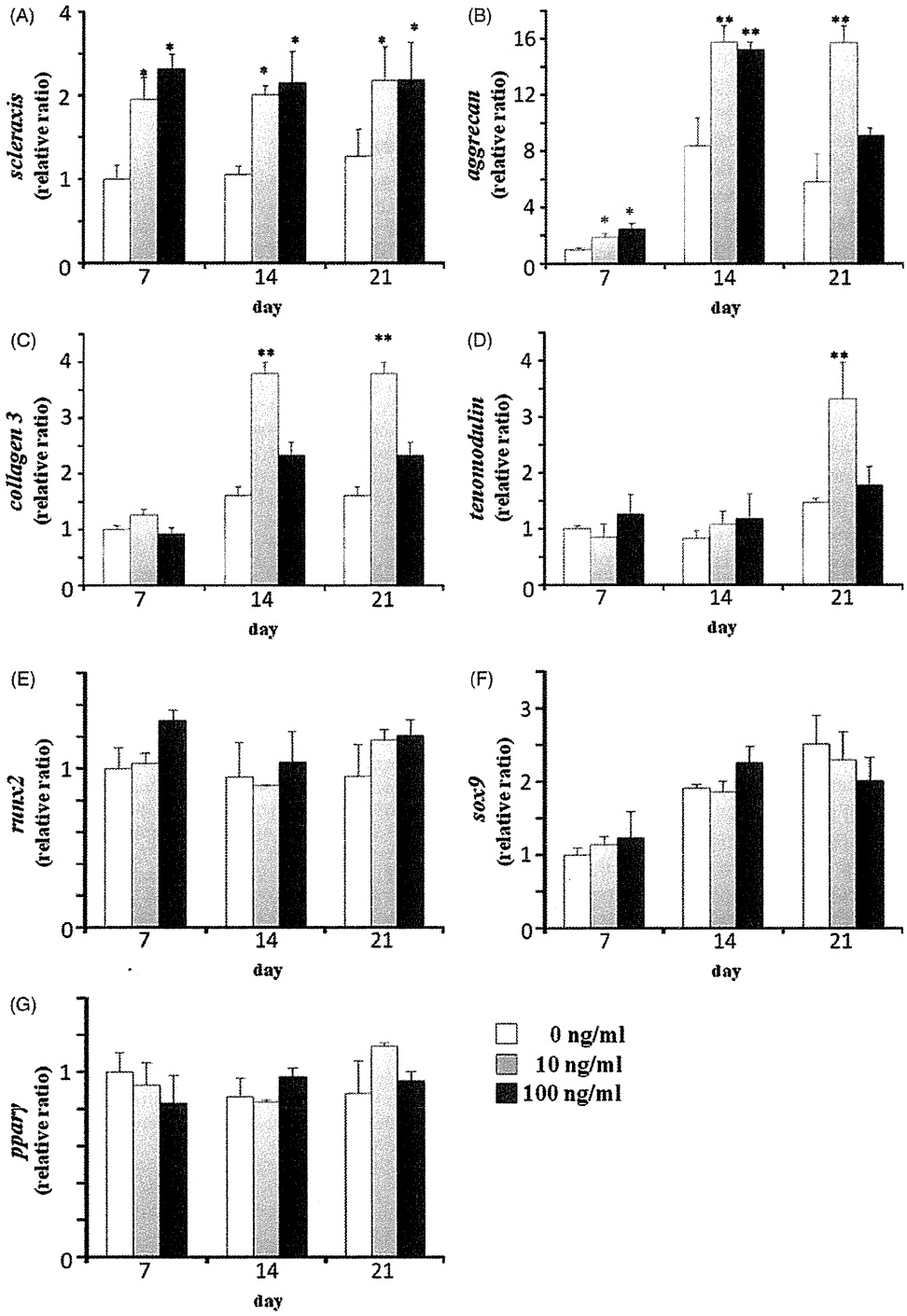

Figure 4. Characteristic changes on P4-6 PDLCs cultured with GDF-5 for 3 weeks. (A–D) Expression levels of *scleraxis* (A), *aggrecan* (B), *collagen 3* (C) and *tenomodulin* (D) mRNAs. (E–G) Expression levels of specific transcription-factors for osteogenic (*runx2*) (E), chondrogenic (*sox9*) (F) and adipogenic (*pparγ*) (G) differentiation. The asterisks represent statistical significance ($*p < 0.05$ and $**p < 0.01$) between the control (cells treated by 0 ng/ml) and the interests (cells treated by 10 and 100 ng/ml).

tenogenic genes, without enhancing the expression of osteogenic, chondrogenic or adipogenic genes. Human PDLCs cultured with GDF-5 showed high expression levels of *scleraxis* from the early phase of culture (7 d). Then, during late phases of culture (14–21 d), PDLCs expressed mature tenocytic *m*RNAs such as *tenomodulin*, *collagen 3*, and *aggrecan*. In particular, PDLCs cultured with 10 ng/ml of GDF-5 maintained high expression levels of these mature tenocytic *m*RNAs when compared with concentrations of 0 and 100 ng/ml GDF-5. For tendon formation, it is known that an inductive interaction between the myotome and sclerotome layers generate the syndetome, demarcated at the earliest stages of development by expression of the basic helix-loop helix transcription-factor gene, *scleraxis* (Towler & Gelbeman, 2006). Therefore, early expression of scleraxis has been considered to be a highly specific marker for

tenogenic differentiation of mesenchymal progenitors (Park et al., 2010; Inoue et al., 2012; Schweitzer et al., 2001). In cultured PDLCs, our previous study demonstrated that *scleraxis* persisted at about the same levels during passages 1 to 6, while the expressions of mature tenogenic genes, such as *tenomodulin* or *collagen 12*, decreased gradually during passages (Itaya et al., 2009). Results from this study showed that GDF-5 treated PDLCs maintained approximately a 2-fold increase in the expression of *scleraxis* for over 3 weeks of culture, when compared with non-treated PDLCs. This reinforced expression of *scleraxis* in PDLCs might have induced the increased expression of *tenomodulin*, a mature tenogenic gene, at late phase of culture. It has been reported that *scleraxis* can upregulate *tenomodulin* expression in tenocytic progenitor cells (Park et al., 2010; Shukunami et al., 2006). PDLCs treated by GDF-5, especially 10 ng/ml in concentration, expressed a 2–3-fold increase in *collagen 3* or *aggrecan* at late phase of culture. This result indicated that GDF-5 might be able to directly enhance the production of these extracellular matrix (ECM) components of tendon fiber from PDLCs. Actually, tendon tissue is composed of tenocytes, collagen fibrils and ECM components (Park et al., 2010). Regarding such components, it has been suggested that collagen 3 has a role in endotenon and epitenon formation (Wang et al., 2005), and aggrecan, a proteoglycan of tendon ECM components, is localized to the compressed segments of tendons (Park et al., 2010; Rees et al., 2000). These data demonstrated that proper concentration of GDF-5 protein could induce a tenocytic differentiation of PDLCs accompanied with increased collagen and proteoglycan production in culture. In contrast, the significant changes of mRNA expressions in cells treated by GDF-7 were not observed in this study. It is known that GDF-7 does not induce bone or cartilage formation, and subcutaneous GDF-7 implantation induced the formation of tendon-like tissues in a rat model (Wang et al., 2005). Although the functions of GDF-7 on cultured PDLCs are not clear in this study, the role of this factor must be involved in the tenogenic differentiation of PDLCs. At least, as mentioned above, GDF-7 cooperates with GDF-5 for the inhibition of osteogenic differentiation in cultured PDLCs.

In conclusion, our findings strongly indicated that supplementation of GDFs in culture could induce periodontal ligament cells into a highly useful cell source for tendon/ligament tissue engineering. In addition, these PDLCs may regenerate both the periodontal ligament tissue as well as tendons/ligaments. Additional investigations will be needed to understand the practical usefulness of PDLCs and GDFs for reliable tendon/ligament tissue engineering.

Declaration of interest

This work was supported by grants from the National Natural Science Foundation of China (81141010 to D.S. Xia), the National Basic Research Program of China (No. 2010CB944801) and the Grant from Beijing Municipal Science and Technology Commission (Z121100005212004), and partially supported by the Grand-in-Aid for Scientific Research (22390375) from Japan Society for the Promotion of Science and Canada Research Chairs, Natural Sciences and Engineering Research Council (NSERC) of Canada. The authors report no conflicts of interest. The authors alone are responsible for the content and writing of the paper.

References

Bolt P, Clerk AN, Luu HH, Kang Q, Kummer JL, Deng ZL, Olson K, et al. 2007. BMP-14 gene therapy increase tendon tensile strength in a rat model of Achilles tendon injury. J Bone Joint Surg Am 89: 1315–1320.

Cabral M, Costa MA, Fernandes MH. 2007. In vitro models of periodontal cells: Comparative study of long term gingival, periodontal ligament and alveolar bone cell cultures in the presence of beta-glycerophosphate and dexamethasone. J Mater Sci Mater Med 18:1079–1088.

Chan SC, Hoang B, Thomas JT, Vukicevic S, Luten FP, Ryba NJ, Kozak CA, et al. 1994. Cartilage-derived morphogenetic proteins. New members of the transforming growth factor-beta superfamily predominantly expressed in long bones during human embryonic development. J Biol Chem 269:28227–28234.

Chung IH, Yamaza T, Zhao H, Choung PH, Shi S, Chai Y. 2009. Stem cell property of postmigratory cranial neural crest cell their utility in alveolar bone regeneration and tooth development. Stem Cells 27: 866–877.

Dines JC, Weber L, Razzano P, Prajapati R, Timmer M, Bowman S, Bonasser L, et al. 2007. The effect of growth differentiation factor-5-coated sutures on tendon repair in a rat model. J Shoulder Elbow Surg 16:S215–S221.

Erlacher L, Ng CK, Ullrich R, Krieger S, Luyten FP. 1998. Presence of cartilage-derived morphogenetic proteins in articular cartilage and enhancement of matrix replacement *in vitro*. Arthritis Rheum 41: 263–273.

Faiyaz-UI-Haque M, Ahmad W, Wahab A, Haque S, Azim AC, Zaidi SH, Teebi AS, et al. 2002. Frameshift mutation in the cartilage-derived morphogenetic protein 1 (CDMP1) gene and sever acromesomelic chondrodysplasia resembling Grebe-type chondrodysplasia. Am J Med Genet 111:31–37.

Fan Z, Yamaza T, Lee JS, Yu J, Wang SL, Fan G, Shi S, Wang CY. 2009. BCOR regulates mesenchymal stem cell function by epigenetic mechanisms. Nat Cell Biol 11:1002–1009.

Forslund C, Rueger D, Aspenberg P. 2003. A comparative dose-response study of cartilage-derived morphogenetic protein (CDMP)-1, -2 and -3 for tendon healing in rats. J Orhop Res 21:617–621.

Gott M, Ast M, Lane LB, Schwartz JA, Chatanzano A, Razzano P, Grande DA. 2011. Tendon phenotype should dictate tissue engineering modality in tendon repair: A review. Discov Med 12:75–84.

Hiraga T, Ninomiya T, Hosoya A, Takahashi M, Nakamura H. 2009. Formation of bone-like mineralized matrix by periodontal ligament cells in vivo: A morphological study in rats. J Bone Miner Metab 27: 149–157.

Ikeda H, Sumita Y, Ikeda M, Ikeda H, Okumura T, Sakai E, Nishimura M, Asahina I. 2011. Engineering bone formation from human dental pulp- and periodontal ligament-derived cells. Ann Biomed Eng 39: 26–34.

Inoue M, Ebisawa K, Itaya T, Sugito T, Yamawaki-Ogata A, Sumita Y, Wadagaki R, et al. 2012. Effect of GDF-5 and BMP-2 on the expression of tendo/ligamentogenesis-related markers in human PDL-derived cells. Oral Dis 18:206–212.

Itaya T, Kagami H, Okada K, Ymawaki A, Narita Y, Inoue M, Sumita Y, Ueda M. 2009. Characcteristic changes of periodontal ligament-derived cells during passage. J Periodontal Res 44:425–433.

Kim TG, Wikesjo UM, Cho KS, Chai JK, Pippig SD, Siedler M, Kim CK. 2009. Periodontal wound healing/regeneration following implantation of recombinant humam growth/differentiation factor-5 (rhGDF-5) in an absorbable collagen sponge carrier into one-wall intrabony defects in dogs: A dose-range study. J Clin Periodontol 36:589–597.

Kwon DH, Bennett W, Herberg S, Bastone P, Pippig S, Rodriguez NA, Susin C, Wikesjo UM. 2010. Evaluation of an injectable rhGDF-5/PLGA construct for minimally invasive periodontal regenerative procedures: A histological study in the dog. J Clin Periodontal 37: 390–397.

Lee JS, Wikesjo UM, Jung UW, Choi SH, Pippig S, Siedler M, Kim Ck. 2010. Periodontal wound healing/regeneration following implantation of recombinant human growth/differentiation factor-5 in a

beta-tricalcium phosphate carrier into one-wall intrabony defects in dogs. J Clin Periodontol 37:382–389.
Lin Z, Rios HF, Park CH, Taut AD, Jin Q, Sugai JV, Robbins PD, Giannobile WV. 2013. LIM domain protein-3 (LMP3) cooperates with BMP7 to promote tissue regeneration by ligament progenitor cells. Gene Ther 20:1–6.
Lowry OH. 1955. Micromethods for the assay of enzyme. II. Specific procedures. Alkaline phosphatase. Methods Enzymol 4:371–372.
Merino R, Macias D, Ganan Y, Economides AN, Wang X, Wu Q, Stahl N, et al. 1999. Expression and function of Gdf-5 during digit skeletogenesis in the embryonic chick leg bud. Dev Biol 206:22–45.
Miyoshi Y. 2002. The expression of growth and differentiation factor (GDF)-7 gene during the development and remodeling of the hard tissues. Shikoku Dent Res 15:139–153.
Morotome Y, Goseki-Sone M, Ishikawa I, Oida S. 1998. Gene expression of growth and differentiation factor-5, -6, -7 in developing bovine tooth at the root forming stage. Biochem Biophys Res Commum 244: 85–89.
Nakamura T, Matuo Y, Tamura M, Izumi Y. 2003. Effects of growth/differentiation factor-5 on human periodontal ligament cells. J Periodont Res 38:597–605.
Nakase T, Sugamoto K, Miyamoto T, Tsumaki N, Luyten FP, Inui H, Myoui A, et al. 2002. Activation of cartilage-derived morphogenetic protein-1 in torn rotator cuff. Clin Orthop Relat Res 399:140–145.
Park A, Hogan MV, Kesturu GS, James R, Balian G, Chhabra AB. 2010. Adipose-derived mesenchymal stem cells treated with growth differentiation factor-5 express tendon-specific markers. Tissue Eng Part A 16:2941–2951.
Rees SG, Flannery CR, Little CB, Hughes CE, Caterson B, Dent CM. 2000. Catabolism of aggrecan, decorin and biglycan in tendon. Biochem J 350:181–188.
Rodrigues MT, Reis RL, Gomes ME. 2013. Engineering tendon and ligament tissues: Present developments towards successful clinical products. J Tissue Eng Regen Med 7:673–686.
Saito Y, Yoshizawa F, Takizawa F, Ikegame O, Ishibashi K, Okuda K, Hara K, et al. 2002. A cell line with characteristics of the periodontal ligament fibroblasts is negatively regulated for mineralization and runx2/cbfa1/osf2 activity, part of which can be overcome by bone morphogenetic protein-2. J Cell Sci 115:4192–4200.
Schweitzer R, Chyung JH, Mutaugh LC, Brent AE, Rosen V, Olson EN, Lassar A, Tabin CJ. 2001. Analysis of the tendon cell fate using scleraxis, a specific marker for tendons and ligaments. Development 128:3855–3866.
Sena K, Morotome Y, Baba O, Terashima T, Takano Y, Ishikawa I. 2003. Gene expression of growth differentiation factors in the developing periodontium of rat molars. J Dent Res 82:166–171.
Seo BM, Miura M, Gronthos S, Bartold PM, Brahim J, Young M, Robey PG, et al. 2004. Investigation of multipotent postnatal stem cell from human periodontal ligament. Lancet 364:149–155.
Settle Jr SH, Rountree RB, Sinha A, Thacker A, Higgins K, Kingsley DM. 2003. Multiple joint and skeletal patterning defects caused by single and double mutations in the mouse Gdf6 and Gdf5 genes. Dev Biol 254:116–130.
Shi S, Bartold PM, Miura M, Seo BM, Robey PG, Gronthos S. 2005. The efficacy of mesenchymal stem cells to regenerate and repair dental structures. Orthod Craniofac Res 8:191–199.
Shukunami C, Takimoto A, Oro M, Hiraki Y. 2006. Scleraxis positively regulates the expression of tenomodulin, a differentiation marker of tenocytes. Dev Biol 298:234–247.
Smith L, Xia Y, Galatz LM, Genin GM, Thomopoulos D. 2012. Tissue-engineering strategies for the tendon/ligament-to-bone insertion. Connect Tissue Res 53:95–105.
Stavropoulos A, Windisch P, Gera I, Capsius B, Sculean A, Wikesjo UM. 2009. A phase IIa randomized controlled clinical and histological pilot study evaluating rhGDF-5/β-TCP for periodontal regeneration. J Clin Periodontol 38:1044–1054.
Stom EE, Kingsley DM. 1996. Joint patterning defects caused by single and double mutations in members of the bone morphogenetic protein (BMP) family. Development 122:3969–3979.
Storm EE, Kingsley DM. 1999. GDF5 coordinates bone and joint formation during digit development. Dev Biol 209:11–27.
Storm EE, Huynh TV, Copeland NG, Jankins NA, Kingsley DM, Lee SJ. 1994. Limb alterations in brachypodism mice due to mutations in a new member of the TGF beta-superfamily. Nature 368:639–643.
Sumita Y, Honda MJ, Ueda M, Asahina I, Kagami H. 2010. Differential effects of growth differentiation factor-5 on porcine dental papilla- and follicle-derived cells. Growth Factors 28:56–65.
Tan SL, Ahmad TS, Merican AM, Abbas AA, Ng WM, Kamarul T. 2012. Effect of growth differentiation factor 5 on the proliferation and tenogenic differentiation potential of human mesenchymal stem cells in vitro. Cells Tissues Organs 196:325–338.
Thomas JT, Lin K, Nandedkar M, Camargo M, Cervenka J, Luyten FP. 1996. A human chondrodysplasia due to a mutation in a TGF-beta superfamily member. Nat Genet 12:315–317.
Towler DA, Gelbeman RH. 2006. The alchemy of tendon repair: A primer for the (S)mad scientist. J Clin Invest 116:863–866.
Wang Q, Chen Z, Piao Y. 2005. Mesenchymal stem cells differentiate into tenocytes by bone morphogenetic protein (BMP) 12 gene transfer. J Biosci Bioeng 100:418–522.
Wolfman NM, Hattersley G, Cox K, Celeste AJ, Nelson R, Yamaji N, Dube JL. 1997. Ectopic induction of tendon and ligament in rats by growth and differentiation factors 5, 6, 7, members of the TGF-β gene family. J Clin Invest 100:321–330.
Yoki T, Saito M, Kiyono T, Iseki S, Kosaka K, Nishida E, Tsubakimoto T, et al. 2007. Establishment of immortalized dental follicle cells for generating periodontal ligament in vivo. Cell Tissue Res 327:301–311.
Zhao M, Xiao G, Berry JE, Franceschi RT, Reddi A, Somerman M. 2002. Bone morphogenetic protein 2 induces dental follicle cells to differentiate toward a cementoblast/osteoblast phenotype. J Bone Miner Res 17:144–151.

Supplementary material available online
Appendix Table

OPEN ACCESS Freely available online

PLOS | ONE

Morphology-Based Prediction of Osteogenic Differentiation Potential of Human Mesenchymal Stem Cells

Fumiko Matsuoka[1☯], Ichiro Takeuchi[2☯], Hideki Agata[3], Hideaki Kagami[3,4], Hirofumi Shiono[5], Yasujiro Kiyota[5], Hiroyuki Honda[1], Ryuji Kato[1,6*]

1 Department of Biotechnology, Graduate School of Engineering, Nagoya University, Nagoya, Aichi, Japan, **2** Department of Engineering, Nagoya Institute of Technology, Nagoya, Aichi, Japan, **3** Tissue Engineering Research Group, Division of Molecular Therapy, The Institute of Medical Science The University of Tokyo, Tokyo, Japan, **4** Department of Oral and Maxillofacial Surgery, Matsumoto Dental University School of Dentistry, Shiojiri, Nagano, Japan, **5** Nikon Corporation, Tokyo, Japan, **6** Department of Basic Medicinal Sciences, Graduate School of Pharmaceutical Sciences, Nagoya University, Nagoya, Aichi, Japan

Abstract

Human bone marrow mesenchymal stem cells (hBMSCs) are widely used cell source for clinical bone regeneration. Achieving the greatest therapeutic effect is dependent on the osteogenic differentiation potential of the stem cells to be implanted. However, there are still no practical methods to characterize such potential non-invasively or previously. Monitoring cellular morphology is a practical and non-invasive approach for evaluating osteogenic potential. Unfortunately, such image-based approaches had been historically qualitative and requiring experienced interpretation. By combining the non-invasive attributes of microscopy with the latest technology allowing higher throughput and quantitative imaging metrics, we studied the applicability of morphometric features to quantitatively predict cellular osteogenic potential. We applied computational machine learning, combining cell morphology features with their corresponding biochemical osteogenic assay results, to develop prediction model of osteogenic differentiation. Using a dataset of 9,990 images automatically acquired by BioStation CT during osteogenic differentiation culture of hBMSCs, 666 morphometric features were extracted as parameters. Two commonly used osteogenic markers, alkaline phosphatase (ALP) activity and calcium deposition were measured experimentally, and used as the true biological differentiation status to validate the prediction accuracy. Using time-course morphological features throughout differentiation culture, the prediction results highly correlated with the experimentally defined differentiation marker values ($R>0.89$ for both marker predictions). The clinical applicability of our morphology-based prediction was further examined with two scenarios: one using only historical cell images and the other using both historical images together with the patient's own cell images to predict a new patient's cellular potential. The prediction accuracy was found to be greatly enhanced by incorporation of patients' own cell features in the modeling, indicating the practical strategy for clinical usage. Consequently, our results provide strong evidence for the feasibility of using a quantitative time series of phase-contrast cellular morphology for non-invasive cell quality prediction in regenerative medicine.

Citation: Matsuoka F, Takeuchi I, Agata H, Kagami H, Shiono H, et al. (2013) Morphology-Based Prediction of Osteogenic Differentiation Potential of Human Mesenchymal Stem Cells. PLoS ONE 8(2): e55082. doi:10.1371/journal.pone.0055082

Editor: Beatriz Pelacho, Foundation for Applied Medical Research, Spain

Received October 8, 2012; **Accepted** December 18, 2012; **Published** February 21, 2013

Funding: We are grateful to the New Energy and Industrial Technology Development Organization (NEDO) for the Grant for Industrial Technology Research (Financial Support to Young Researchers, 09C46036a) for the support. The research was also supported in part by a grant-in-aid from Nikon Corporation. The funders had no role in study design, data collection and analysis, decision to publish, or preparation of the manuscript.

Competing Interests: We have the following interests. This study was supported in part by a grant-in-aid from Nikon Corporation. Hirofumi Shiono and Yasujiro Kiyota are employed by Nikon Instruments. Ryuji Kato is one of the main investigators of 12 patents (pending) related to basic technologies of "algorithms of cellular image processing. Hirofumi Shiono, is one of the inventors of the hardware we used in our research, "BioStaion CT" which is the automatic cell culture system, and a member of this collaborative project with Nagoya Univ. The BioStation CT and relating software are marketed products of Nikon Corporation. Although the system and the software were used in this study, the result of this research does not depend on the system and the software. He is one of the inventors of related 12 patents. Yasujiro Kiyota, is one of the inventors of the hardware we used in our research work. There are no further patents, products in development or marketed products to declare. This does not alter our adherence to all the PLoS ONE policies on sharing data and materials, as detailed online in the guide for authors.

* E-mail: kato-r@ps.nagoya-u.ac.jp

☯ These authors contributed equally to this work.

Introduction

Mesenchymal stem cells (MSCs) are a useful cell source for tissue engineering and regenerative medicine of various tissues because of their multi-lineage differentiation capacity (e.g., osteogenic, chondrogenic, adipogenic, neurogenic, and myogenic) [1–3]. Although MSCs can be harvested from various tissues, including adipose tissue and dental pulp, bone marrow derived MSCs (BMSCs) have a well-described *in vivo* bone-forming capacity and are widely used for clinical bone regenerative therapies [4–6]. Several groups, including ours, have been successful in clinical bone tissue engineering using human bone marrow mesenchymal stem cells (hBMSCs) [7–9]. In spite of documented clinical successes of bone regeneration with hBMSCs,

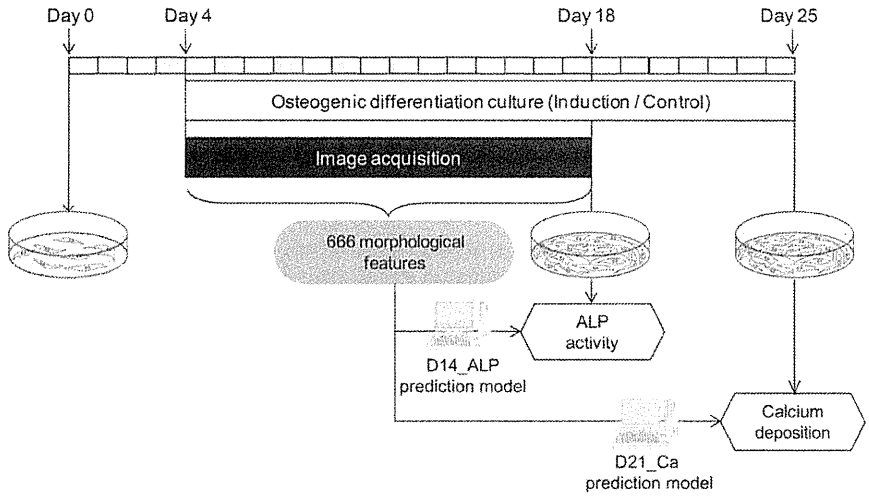

Figure 1. Schematic illustration of the experimental scheme for the prediction of osteogenic differentiation potential using multiple and time-course morphological features. hBMSCs were cultured in non-induction medium in first 4 days, then the medium was replaced with osteogenic induction medium only for the Induction sample. From day 0 to day 14, cell images were automatically acquired by BioStation CT every 8 hours. ALP activity and calcium deposition rates were evaluated on days 14 and 21, respectively. Using multiple morphological features covering 2 weeks culture, two types of hBMSC osteogenic differentiation evaluation results were predicted by individual prediction models.
doi:10.1371/journal.pone.0055082.g001

robust therapeutic efficacy able to withstand the large variation among patients remains a challenge. Therefore, practical and effective cell-quality assurance methods are a necessary approach to address the unmet need of minimizing variability in patient outcomes.

Previous works aimed at characterizing BMSC osteogenic potential have mainly focused on methods that damage cells (e.g., staining, gene expression, etc.) [10]. These conventional techniques limit clinical translation in two ways. First, the destructive nature of the measurements consumes cellular material that would otherwise be useful for therapy. Second, the sample measurements are terminal endpoints, in part due to the irreversible damage incurred by the cells from the measurement procedure. As a result, repeated measurement on the same cellular sample is not possible and longitudinal sampling consumes more material.

Currently, the daily monitoring of cellular morphology by microscopy is combined with minimum sampling for biochemical markers to serve as the routine cellular quality assessment during the expansion culture process. Qualitative microscopic examination and the consumptive nature of the biochemical assays impose a limit on the predictive control currently available in clinical practice. A quantitative, non-invasive method for predicting cellular osteogenic potential and quality is needed to better anticipate clinical outcomes.

Cellular morphology has historically been used as an important indicator to characterize present and assess cell quality. Several reports describe correlations between osteogenic differentiation potential and cellular morphology. Kelly *et al.* have reported that cell geometry is highly correlated with differentiation into osteogenic lineages [11]. Takagi *et al.* have also reported that the cell roundness of hBMSCs is highly correlated with the expression of osteogenic differentiation marker genes [12]. In addition to the above examples that match morphology and cell potential, there are increasing numbers of reports describing image-based cell assessment methods. The popularity of fluorescence-labeled imaging methods in high content cellular screening has outpaced methods with non-labeled image-based assessment; however these approaches retain some technical drawbacks, which do not necessarily improve upon the non-labeled methods [13–16].

In this study, we aimed to demonstrate the efficacy of the non-invasive prediction model, which only uses cellular morphology features to forecast the osteogenic differentiation potential of hBMSCs. Specifically, the outcomes of two biochemical osteogenic markers were quantitatively forecast by two types of prediction models: (1) the alkaline phosphatase (ALP) activity 14 days after differentiation, designated as "D14_ALP model", and (2) the calcium deposition rate 21 days after differentiation, designated as "D21_Ca model". ALP activity is a BMSC differentiation marker; however measuring ALP activity alone is not sufficient for predicting *in vivo* bone formation. Compared to ALP, calcium deposition rate is an osteogenic differentiation marker that highly correlates with *in vivo* bone formation. However, since calcium deposition is a late phenotypic marker, which appears beyond the optimal implantation stage, it is not commonly applied as a clinically useful marker. Overall, it is impossible to measure both markers with the same cell sample or quantitatively predict the measurement results using conventional methods.

To advance this field, we aimed to investigate whether a morphology-based prediction model is capable of quantitatively predicting both ALP activity and calcium deposition rate. Further on, to demonstrate the clinical feasibility of our resulting morphology-based prediction models we examined practical considerations for use in the clinic in order to predict osteogenic potential for new patients scheduled for cell therapy. Two simulation scenarios were carefully examined: (Scenario I) Prediction of osteogenic differentiation potential of a new patient's cells by a model trained with historical patient data; (Scenario II) Prediction of osteogenic differentiation potential of a new patient's cells by a combination of historical patient data and partial culture imaging data from the early stage expansion of the new patient's own cells.

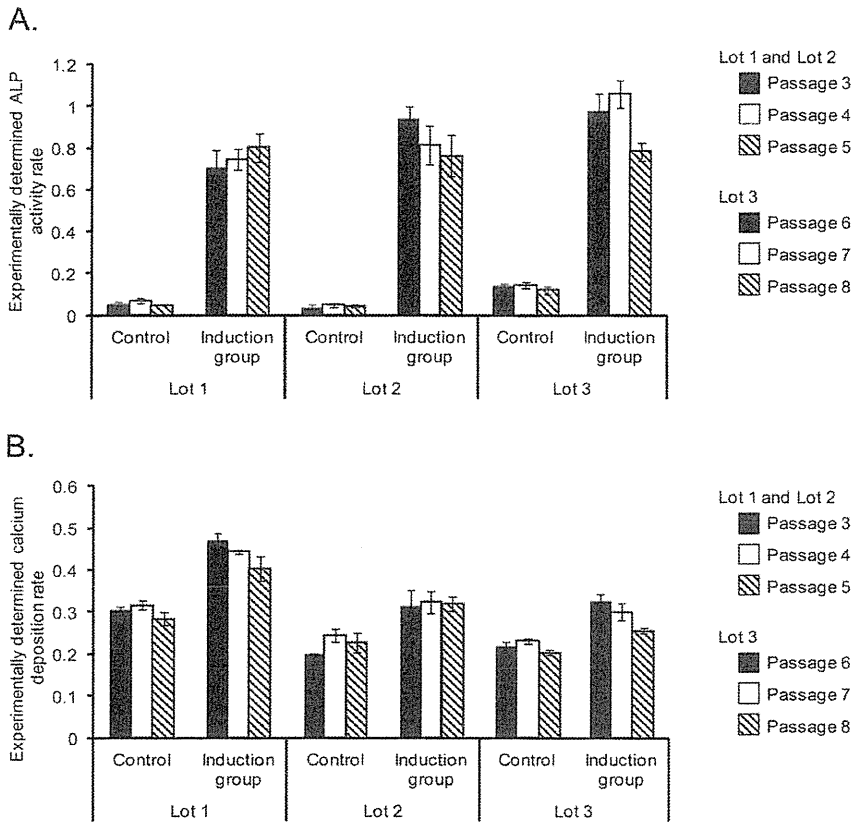

Figure 2. Experimentally determined biological results after the osteogenic differentiation. A: Experimentally determined ALP activity rate on day 14 of differentiation. B: Experimentally determined calcium deposition rate on day 21 of differentiation.
doi:10.1371/journal.pone.0055082.g002

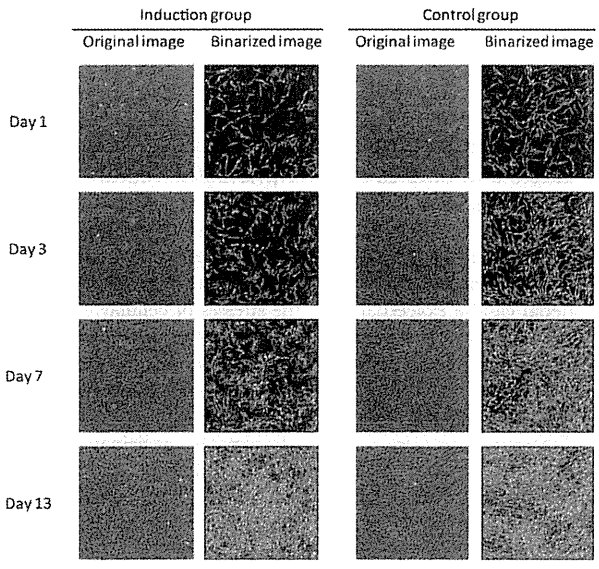

Figure 3. Phase contrast raw image from BioStation CT and its processed image. The images of beginning (day 1), middle (day 3 and 7), and the end (day 13) in the induction period of Lot 1 are indicated as examples. Raw images were binarized with MetaMorph.
doi:10.1371/journal.pone.0055082.g003

Results

Biological/morphological changes during osteogenic differentiation culture

hBMSCs were either cultured in differentiation induction medium or in non-induction medium according to the protocol illustrated in Fig. 1, which was based on the clinical jaw bone therapy protocol used by our group [7]. Three lots of cells, passaged three times per lot, were used to assess "patient-derived variance" and "processing-derived variance." After the image acquisition period during differentiation culture, ALP activity was measured from the same well that the images were acquired. After an additional week of differentiation culture, calcium deposition rate was quantified.

All cell lots at all passages in the induction groups showed a clear increase in ALP activity compared to the control groups (Fig. 2–A). The calcium deposition rate was also significantly higher in the induction group than the control group among all lots and all passages (Fig. 2–B). However, greater variation was observed in the calcium deposition assays compared to the ALP assays. This result reflects the fact that ALP activity measurements add information of osteognic differentiation, but does not qualify as a marker of further osteogenic maturation potential even in *in vitro*.

In contrast to biochemical measurements, which exhibited a noticeable pattern after several weeks of culture, a signature pattern using morphological measurements was found within 7 days of differentiation culture (Fig. 3). For all cell lots at the

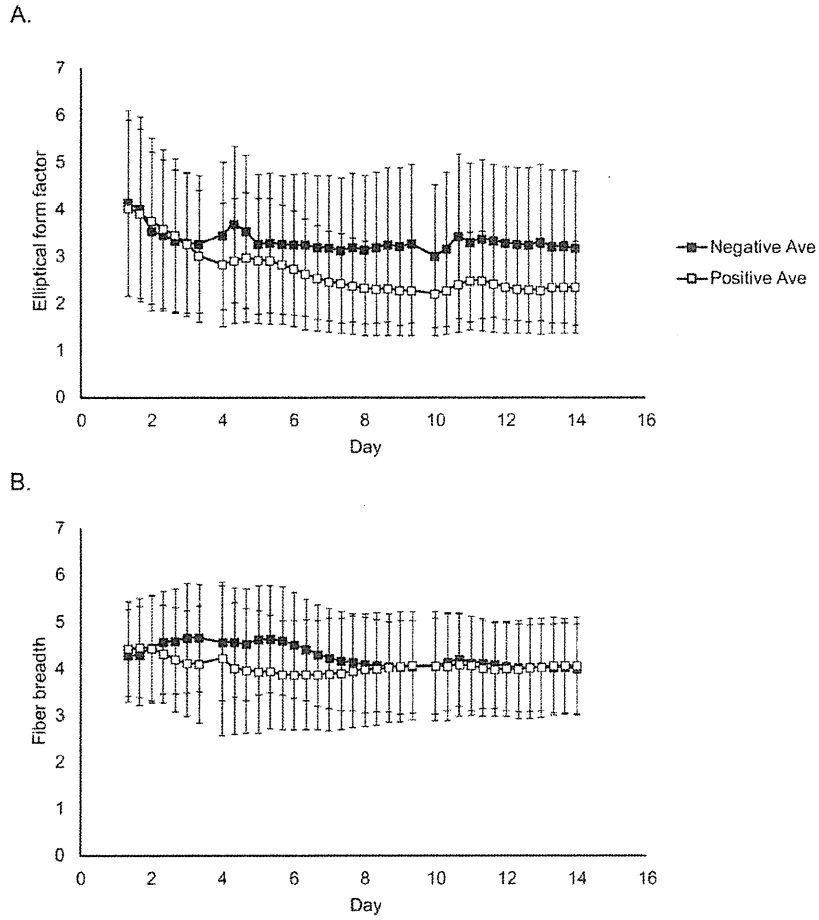

Figure 4. Time series changes of characteristic morphological features. From the 9 morphological features measured, elliptical form factor (A) and fiber breadth (B) of Lot 1 are indicated as representative examples. The symbols indicate the mean value of each morphological feature from all cells in one condition (3 wells ×5 view fields). Roughly, 4,000 to 40,000 cells were measured for the mean. Standard deviations are shown as error bars.
doi:10.1371/journal.pone.0055082.g004

7 day time point, cell morphology in the induction group was observed as flat and spread in multiple two dimensional directions, as compared to the fibroblast-like sharp spindle shape of the control group. By summarizing the quantitative morphological changes in all cells under the same culture conditions through image analysis, an early indication of the cellular phenotype was apparent. For some morphological features, such as Elliptical form factor (the ratio of the object's width to its length) or Fiber breadth (the width of an object modified as a straight fiber), a statistically significant difference ($p<0.01$) between induction and control groups could be identified at a very early culture stage (Fig. 4). Elliptical form factor of Lot 1 was significantly different ($P<0.001$) from day zero at day three of differentiation culture and then throughout the differentiation period. Although these types of morphological differences suggest a relationship to osteogenic induction, they are insufficient to quantitatively predict the final cellular state. To improve predictive power, a machine learning approach was taken to construct a computational model for quantitative prediction and determine the best combination of morphological features to use.

Prediction of osteogenic differentiation potential using multiple and time-course morphological features

Standard practice for bone regeneration therapy is to start by expanding a new patient's cell material to a certain yield, then applies an osteogenic differentiation protocol up until the day of therapy. Variations in the quality of a new patient's starting material can be exacerbated by the stresses of cellular expansion. For these reasons a model for characterizing the regenerative capacity of a patient's cell source, including quality, yield and most importantly osteogenic potential, would add tremendous value to current standard practice.

Two scenarios were designed to simulate anticipated clinical situations available for applying morphology-based prediction models to assess new patient cellular quality. Scenario I: Prediction of new patient BMSC osteogenic potential using a model trained with historical patient data (Fig. 5–A). Scenario II: Prediction of new patient BMSC osteogenic potential using a model trained with historical patient data in addition to data derived from the new patient material (Fig. 5–B). The accuracies of both D14_ALP and D21_Ca models were evaluated in each scenario. Nine morphological features were evaluated from 37 time points over 14 days and complied from 666 image-based input features. The

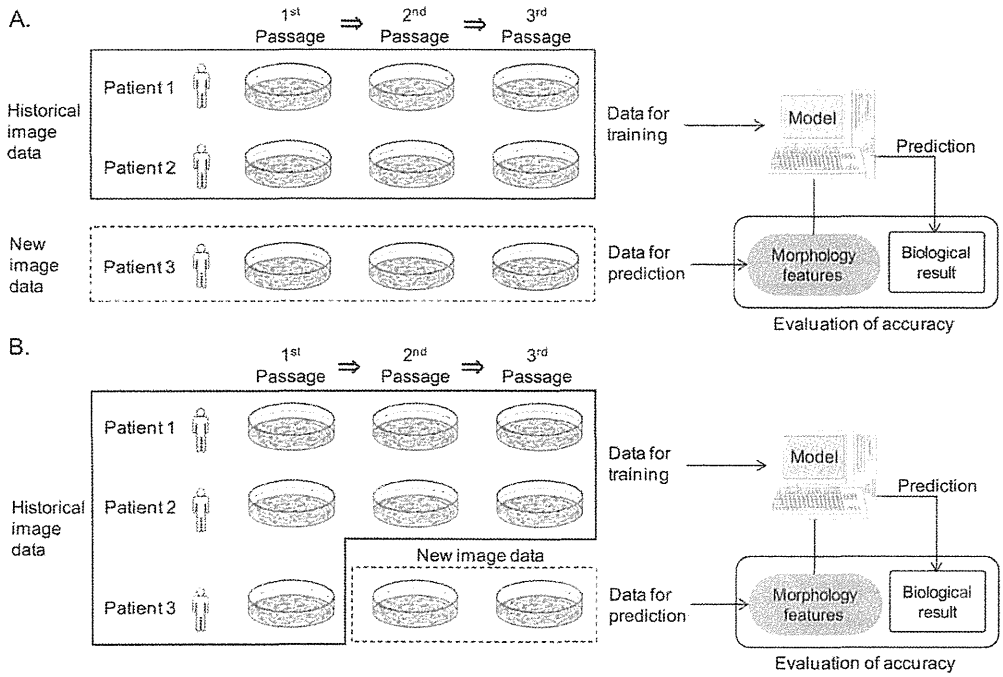

Figure 5. Schematic illustration of two scenarios examined to simulate clinical feasibility. A: (Scenario I) New patient prediction scheme: Trained by historical patient dataset only. Images from all passages of patient 3 were used for prediction. B: (Scenario II) Ongoing patient prediction scheme: Trained by historical patient datasets and a partial dataset from the new patient. For example, for the prediction of cell potential of patient 3, Scheme I uses images of patient 1 and 2 only. Scheme II used images of patient 1 and 2, together with some images from patient 3.
doi:10.1371/journal.pone.0055082.g005

corresponding biochemical differentiation markers from each of the 54 samples were also evaluated. We selected Ridge regression as the machine learning modeling method for linking morphological features to the biomarker measurement results [17]. This method was chosen since Ridge regression is a type of standard regression model that eliminates the multicolinearity problem in multivariate models [18].

Scenario I: New patient prediction scheme. The new patient prediction scheme is designed to simulate the clinical situation where evaluating a new patient's cell quality can be accomplished quickly and reliably (Fig. 5–A). With this scheme, the prediction model can be prepared previously by historical image data from other patients. This model aspires to require no previous data from the new patient.

The prediction accuracies of the D14_ALP and the D21_Ca models are shown in Table 1 and, Fig. 6 (see also Fig. 7 and Table S1 for detailed data). From both prediction results, the correlation coefficients indicated that time-course morphological features of BMSCs during differentiation correlate with the experimentally obtained osteogenic marker values. The average

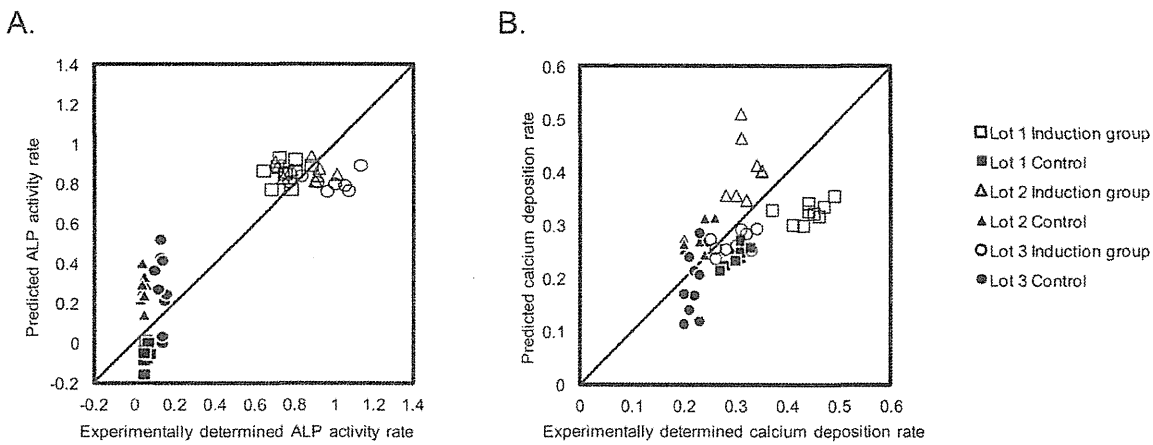

Figure 6. Prediction accuracies in the new patient scheme. A: Scatter plot of experimentally determined values versus predicted values in D14_ALP model, B: Scatter plot of experimentally determined values versus predicted values in D21_Ca model.
doi:10.1371/journal.pone.0055082.g006

Table 1. Prediction accuracy of Ridge regression models for osteogenic differentiation status of hBMSCs.

	New patient prediction scheme		Ongoing patient prediction scheme	
	Ave. absolute prediction error* [−]	R** [−]	Ave. absolute prediction error* [−]	R** [−]
ALP activity rate prediction	0.151	0.903	**0.111**	**0.950**
Calcium deposition rate prediction	0.065	0.526	**0.037**	**0.821**

*Ave. absolute prediction error is the average of the differential between experimentally determined rate and predicted rate.
**Correlation coeffecient between experimentaly determined and predicted rate.
doi:10.1371/journal.pone.0055082.t001

of absolute prediction errors indicates that each prediction model provides predictions within the error rage of ±0.151 with the D14_ALP model and ±0.065 with the D21_Ca model, respectively (Fig. 7). When the variance of all assay data, the result of manual experimental variance, is normalized as 1.0, the prediction errors between different assay measurements can be standardized as 0.194 (D14_ALP) and 0.963 (D21_Ca). This standardized error provides the interpretation that the prediction values are 5-fold stable (D14_ALP) or nearly equal (D21_Ca) compared to the human assay variances.

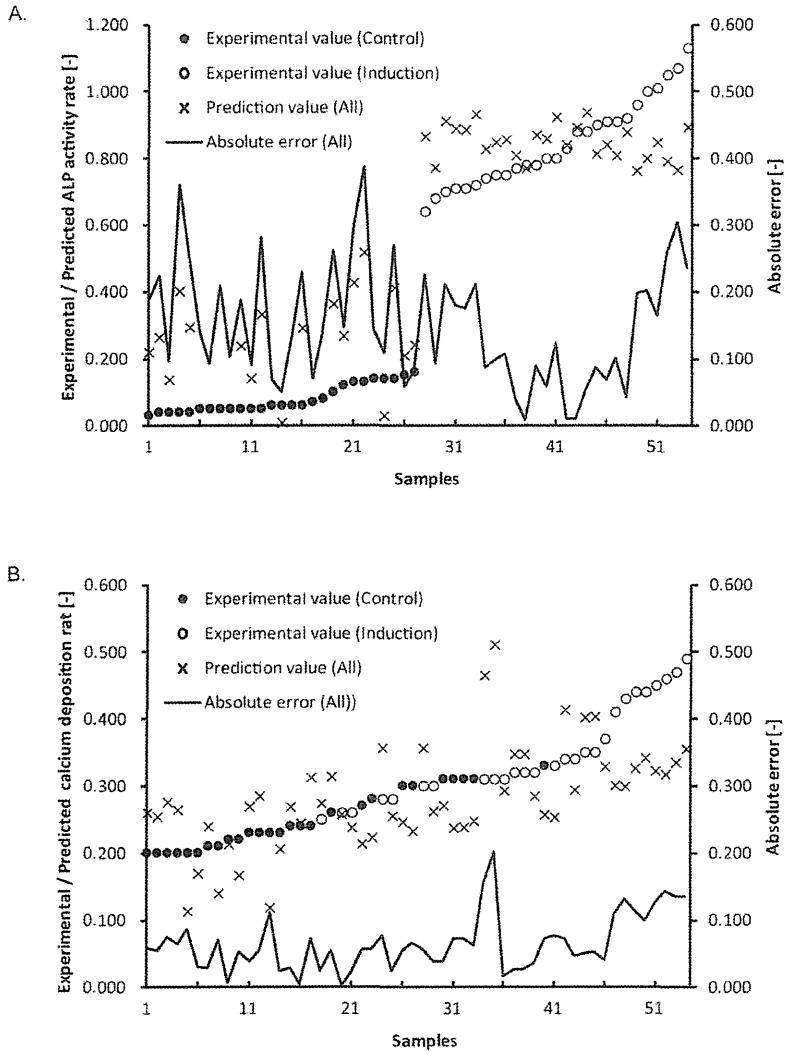

Figure 7. Detailed prediction results in new patient scheme. A: Prediction results and error range in the D14_ALP model. B: Prediction results and error range in the D21_Ca model. All the plotted data were rearranged in the order of experimental values.
doi:10.1371/journal.pone.0055082.g007

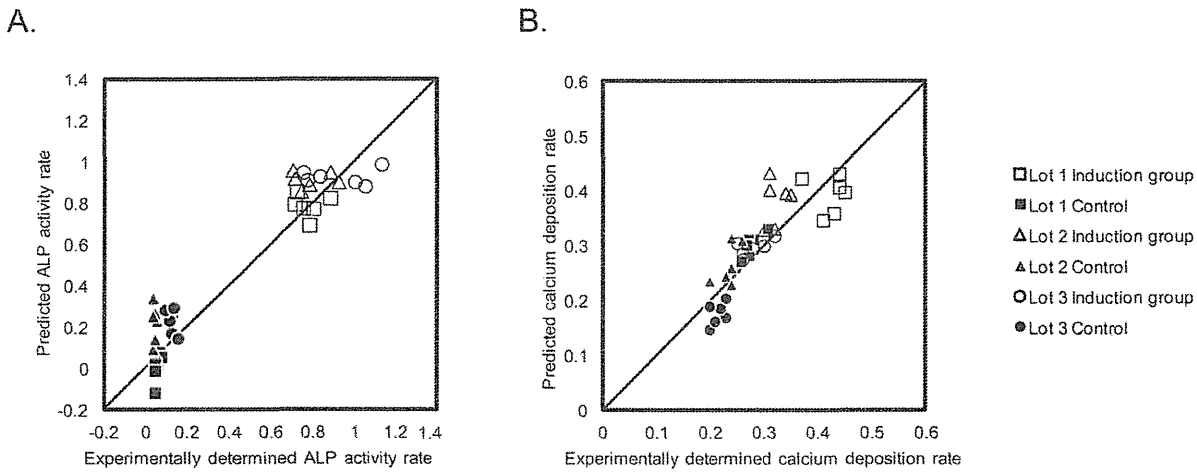

Figure 8. Prediction accuracies in the ongoing patient scheme. A: Scatter plot of experimentally determined values versus predicted values in D14_ALP model, B: Scatter plot of experimentally determined values versus predicted values in D21_Ca model.
doi:10.1371/journal.pone.0055082.g008

Scenario II: Ongoing patient scheme. The ongoing patient prediction scheme is designed to simulate the clinical situation of evaluating a new patient's cell quality with higher accuracy in return for additional data acquisition process (Fig. 5–B). With this scheme, a small sample of the new patient's cells should be differentiated for 14 days as a pilot culture in parallel to the expansion culture. During this pilot culture, cell images are taken to represent the new patient's cellular characteristics. The new patient's data and previous patients' historical data are combined for training the prediction model. Using image data from the next passage and from the 14 day differentiation culture, a prediction can be made prior to the cell harvest (Fig. 5–B). The advantage of this scheme is inclusion of new patient data at the cost of acquiring and inputting new patient images. Characteristics, which may be unique to the new patient, can then be incorporated into training the model with the expectation of a greater predictive value.

The prediction results of the D14_ALP and D21_Ca models are shown in Table 1 and Fig. 8 (see also Fig. 9 and Table S2 for detailed data). These results confirm that the morphological features of hBMSCs observed during differentiation culture highly correlates with the future osteogenic potential. The error ranges were tightened to ± 0.111 with D14_ALP model, and ± 0.037 with D21_Ca model (Fig. 9) as compared to using only historical data to train the model. The standardization of all assay variances to 1.0 results in prediction errors of 0.110 (D14_ALP) and 0.333 (D21_Ca) respectively. Overall, these results suggest that prediction values from Scenario II morphology-based models are nearly 9-fold stable (D14_ALP) or 3-fold stable (D21_Ca) compared to the human assay variances.

When comparing the two scenarios, the prediction accuracies in both prediction models (D14_ALP and D21_Ca) greatly improved in Scenario II, the ongoing patient prediction scheme. These results indicate that incorporation of morphological characteristics from the patient's own cells is extremely important and informative for predicting an individual's BMSC osteogenic potential.

Discussion

Although qualitative cellular morphology is used as a guide for estimating osteogenic differentiation, a quantitative relationship between cellular morphology and biochemical osteogenic markers is not well established. In the present study, we investigated the possibility of predicting osteogenic differentiation of hBMSCs from phase contrast images alone. Specifically, a machine learning algorithm was used to train 14 day cell morphology information and terminal osteogenic biochemical marker values into a model used to predict the terminal marker values from a test set of morphologic data. Our results provide evidence that using this approach can potentially automate and improve decisions, which are currently based on conventional destructive assays and qualitative microscopic assessments.

Using both ALP activity and calcium deposition rates in assessing cellular quality is important to current standard practices. Our proposed modeling schemes allow for accurate prediction of both endpoints. Of particular importance is the accurate prediction of calcium deposition, which is more closely associated with *in vivo* bone formation. For these reasons, constructing different types of prediction models to allow real-time evaluation of the same target cells with multiple aspects and add information for more careful decision making in the culture process. These attributes of an automated computational approach for assessing cellular quality support improvement of safety, efficacy and more rapid and economical scheduling decisions by physicians.

New technology allowing automated image acquisition, which can currently provide more images with greater quality and fewer biases, improves our ability to generate more predictive models based on cellular morphology. In our work, state-of-the art imaging platform (in this study BioStation CT), is the first enhancement technology which lead us to provide uniform and objective data without need for manual optimization of lighting, focusing, or other systematic errors common to manual image acquisition. Operator bias for field selection is also greatly reduced by optimization of the seeding protocol to improve cell distribution together and optimization of the number of fields to view jointly. Image processing biases, the thresholding bias to extract cells from non-cell objects recognized in the images, are also improved by a new automated threshold determination algorithm (data not shown). By preparing three different cell lots and three different passages for cell samples, we aimed to reduce biases of specific patient.

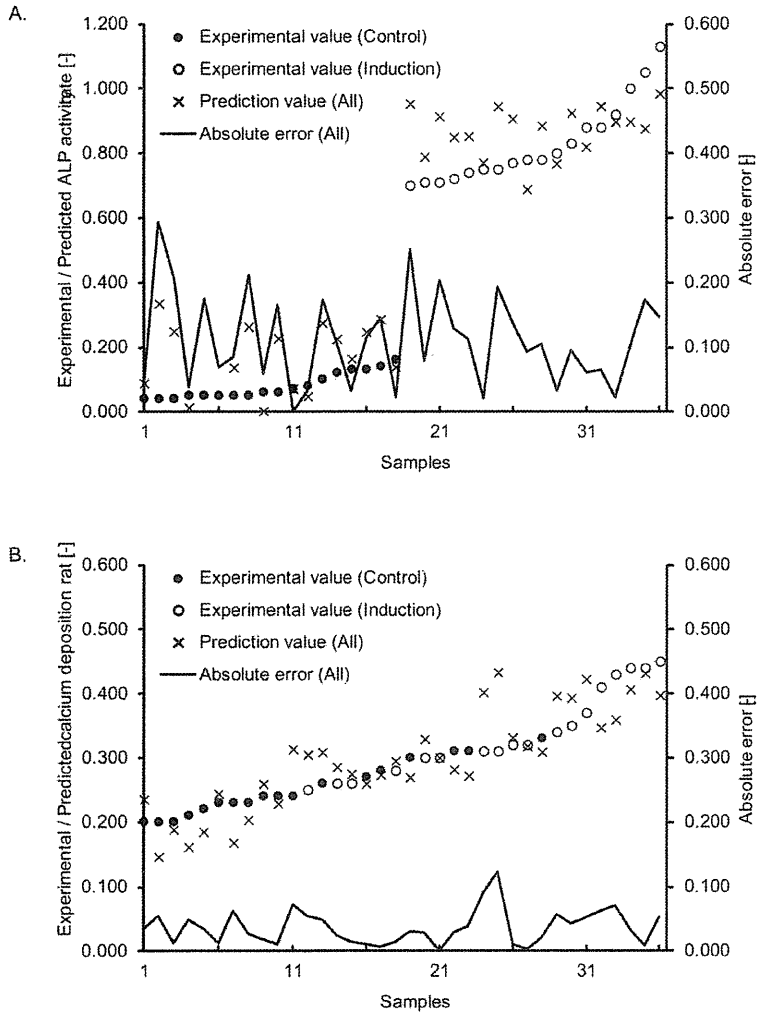

Figure 9. Detailed prediction results in ongoing patient scheme. A: prediction results and error range in the D14_ALP model. B: Prediction results and error range in the D21_Ca model. All the plotted data were rearranged in the order of experimental values.
doi:10.1371/journal.pone.0055082.g009

Table 2. Prediction accuracy of Redge regression models with elimination of each individual features for ALP activity rate.

	New patient prediction scheme		Ongoing patient prediction scheme	
Excluded parameter	**Ave. prediction error* [−]**	**Standardized error** [−]**	**Ave. prediction error* [−]**	**Standardized error** [−]**
Breadth	0.131	0.142	0.078	0.057
Elliptical form factor	0.121	0.124	0.074	0.052
Fiber breadth	0.156	0.197	0.091	0.074
Fiber length	0.136	0.147	0.074	0.051
Hole area	0.141	0.152	0.085	0.060
Inner radius	0.138	0.146	0.088	0.065
Relative hole area	0.134	0.148	0.090	0.065
Shape factor	0.148	0.180	0.108	0.104
Total area	0.136	0.153	0.087	0.064

*Ave. prediction error is the average of the differential between experimentally determined rate and predicted rate.
**Standardized error is calculated by dividing the average of squared errors by variance of all the experimentally evaluated values.
doi:10.1371/journal.pone.0055082.t002

Table 3. Prediction accuracy of Redge regression models with elimination of each individual features for calcium deposition rate.

	New patient prediction scheme		Ongoing patient prediction scheme	
Excluded parameter	**Ave. prediction error* [−]**	**Standardized error** [−]**	**Ave. prediction error* [−]**	**Standardized error** [−]**
Breadth	0.065	0.924	0.028	0.187
Elliptical form factor	0.066	0.972	0.026	0.166
Fiber breadth	0.062	0.870	0.026	0.158
Fiber length	0.065	0.921	0.027	0.164
Hole area	0.065	0.937	0.026	0.138
Inner radius	0.063	0.892	0.028	0.180
Relative hole area	0.060	0.769	0.025	0.146
Shape factor	0.067	0.939	0.029	0.201
Total area	0.067	0.968	0.027	0.160

*Ave. prediction error is the average of the differential between experimentally determined rate and predicted rate.
**Standardized error is calculated by dividing the average of squared errors by variance of all the experimentally evaluated values.
doi:10.1371/journal.pone.0055082.t003

The second enhancement incorporated into this study is the incorporation of robust and continuous morphological features. In this study, it is a key that the morphological features actually used in our modeling are statistical composites (average and standard deviation) of features obtained from all cells from a given condition, which is typically comprised of approximately 4,000–40,000 cells from 15 images for each condition. Such large number of technical replicates offers robustness in each parameter, and effectively enhanced the performance of our prediction model. The continuous image acquisition with precise timing by BioStation CT allowed us to obtain both static morphological features and their dynamic changes throughout the differentiation process. Since morphological changes during osteogenic induction are time-dependent events, it is important to analyze morphological changes with precise timing.

The third enhancement provided by our work stems from the examination of two clinically plausible scenarios. Through these experiments, we found that prediction accuracies of both osteogenic potential measurements greatly increase when the model incorporates training information from early images from the same patient, which reflects individual characteristics in cell morphology. Carefully considering patient-to-patient morphology variation exposes limitations in the current practice of experience-based assessment by culture experts. As indicated in our results, use of new high-content information databases from images, where large amounts of data can be computationally organized and retrieved, is one possible approach for incorporating many aspects related to patient-to-patient variability. Constructing predictive models using historical databases and individualizing new patient predictions by incorporating each new patient's data would be a practical approach to mitigating patient variability while improving the precision of quality assessments.

Comparing the prediction errors of D14_ALP and D21_Ca models in Table 1, the D14_ALP prediction accuracy was higher. One possible explanation for the discrepancy between D14_ALP and D21_Ca predictions is the lack of morphological data during the calcium deposition period, which requires an additional week of culture following two weeks of induction culture. We plan to further investigate ways to enhance predicting this late maturation marker by accumulating more culture images to accrue a larger historical data set. However, we were surprised to discover that without the last seven days of morphology data the D21_Ca model could still predict the final calcium deposition result with reasonable accuracy. To our knowledge, no other reports have been able to accurately estimate the final calcium deposition from early images.

Previous reports have indicated that morphological parameters, similar to the ones used in this study such as flatness or polygonal rate, highly correlate with the osteogenic differentiation potential. Consistent with these reports, we looked at the contribution of each parameter to the prediction performance. In regression analysis, one can examine the effect of each parameter by examining the regression coefficients. Interestingly, among the nine parameters introduced into the regression analysis, there were few sizeable positive or negative coefficients (data not shown). This suggests that there are few dominant morphological parameters that simply correlate to the differentiation potential. Furthermore, when individual features were intentionally eliminated from the model, no significant deterioration was observed in the prediction accuracy (Table 2 and 3). These results suggest that correlation of morphological features and the osteogenic differentiation potential is so complex that there are various compensatory features. Therefore, we conclude that to gain the most robust prediction model for hBMSC osteogenic differentiation potential, all available morphological features throughout the differentiation culture should be incorporated, and biased or feeling-based morphological feature selection should be avoided.

In this work, longitudinal morphological measurements were used as individual, unconnected features, like snapshots. However, to improve the accuracy of the D21_Ca model, we examined ways to incorporate time dependent changes of individual features. With this idea, the same morphological features were converted to change rates between sampling times, analogous to measuring the differences through snapshots. As a result, this morphological feature transformation reduced the D21_Ca model standardized error rate from 0.333 to 0.192 (data not shown). We plan to further investigate the transformation or repeated measurements into time-based trends and patterns in morphological data to improve predictive performance. Our next investigation is designed to further demonstrate applicability and robustness of our proposed method by evaluating the model's ability to characterize "cellular variances", derived from patient diversity, culture protocol effects, and accumulating stresses throughout culture. We also plan to further expand the scope of this work to translate progress made using *in vitro* models and endpoints for morphological prediction of osteogenic potential *in vivo*.

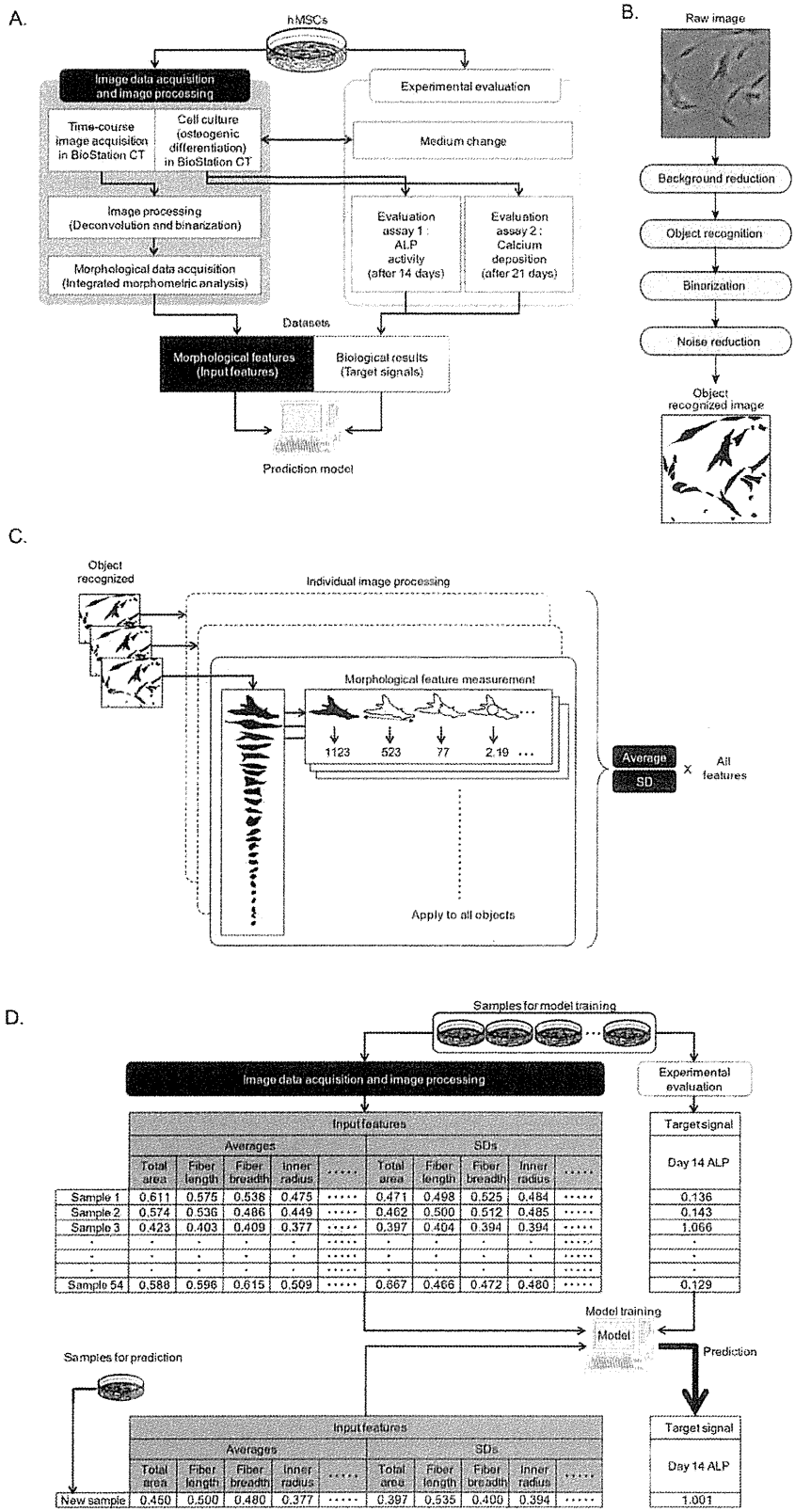

Figure 10. A: Schematic illustration of cell image processing. The raw images were first pre-processed by background reduction processing

by deconvolution and open-close filters. Then, images were binarized by the optimized threshold. The noisy objects were eliminated by particle deletion filter. B: Schematic illustration of cell morphology measurements and data processing. In all object recognized images, all existing objects were measured for the 9 morphological features. Since 1 condition was designed to consist of 3 wells ×5 view fields, all the corresponding object measurement results were processed as a same sample. The average and standard deviation within one sample of all morphological features at each time point were used as the input features for modeling. C: Schematic illustration of prediction model construction. Prediction of differentiation potential consisted of two steps. First, two types of prediction models (D14_ALP model or D21_Ca model) were constructed with the set of image data and experimental evaluation. Second, the values of D14_ALP or the D21_Ca were predicted from the input features of the sample targeted for prediction. The predicted biological rates are compared to the experimentally-determined results to evaluate the accuracy of prediction model.
doi:10.1371/journal.pone.0055082.g010

Materials and Methods

Cells and cell culture

Human bone-marrow derived mesenchymal stem cells (hBMSCs) (Lonza Walkersville, Inc., Maryland, U.S.A.) were subcultured (passaged) in Dulbecco's modified Eagles' medium (DMEM) containing 10% fetal bovine serum (FBS) (Life Technologies Japan Ltd., Tokyo, Japan). Three lots of hBMSCs were designated as Lot 1 (strain number 15000-1, unknown race, Male, 19-year-old), Lot 2 (strain number 17174, Oriental, Male, 20-year-old), and Lot 3 (strain number 11533, Black, Male, 22-year-old), respectively. Lot 1 and 2 were cultured to passages 3, 4, and 5, and Lot 3 was cultured to passages 6, 7, and 8, and cryopreserved for the start of the image acquisition experiment. Cryopreserved cells were seeded at a density of 1.0×10^4 cells/well in 12-well plate (Greiner Bio-One., Frickenhausen, Germany), and the cell-seeding day was designated as day 0 in the image acquisition experiment.

Fig. 1 illustrates the experimental scheme for hBMSC osteogenic differentiation culture. From day 0 to 3, cells were cultured in 10% FBS-containing α-modified Eagle's medium (αMEM) (Sigma-Aldrich Co., St. Louis, MO, U.S.A.). From day 4 to 18, cells were divided into two groups: (1) Osteogenic induction group (Induction, N = 6) and (2) Non-induction group (Control, N = 6). For the induction group, the medium was switched to induction medium consisting of 10% FBS-containing αMEM medium supplemented with 10 nM dexamethasone (Sigma-Aldrich Co.), 100 mM ascorbic acid (Wako Pure Chemical Industries, Ltd., Osaka, Japan), and 10 mM glycerol 2-phosphate sodium salt hydrate (Sigma-Aldrich Co.). For the non-induction group, supplements were not added to the 10% FBS-containing αMEM medium. The appropriate medium was changed at day 7 and day 13. For half of the samples in each experimental group (n = 3), alkaline phosphatase (ALP) activity were quantified on day 18. The remaining samples continued culture until day 25, and calcium deposition was quantified on day 25.

Image acquisition

Figs. 1 and 10-A illustrates the image acquisition scheme during hBMSC osteogenic differentiation culture. From day 0 to day 13 (14 days), phase contrast microscopic images of hBMSCs were obtained using the BioStation CT (Nikon Corporation, Tokyo, Japan). BioStation CT is an automatic cell maintenance system, which maintains a stable incubation environment (37°C, 5% CO_2, 100% humidity) with scheduled automatic image acquisition. The number of view fields was optimized to five, which provides the least error for estimating the correct cell seeding for each well. Five view fields (center position and four positions 2.2 mm from the center) of phase contrast images were acquired from each well with fully automatic focusing. The phase contrast images had the least noise and background when using the halo-reduction lens. Image acquisition timing was set to every 8 hours from day 4 to 18 (magnification = 10x). Time points are designated as time 0 to 38, indicating each of the 8 hour imaging intervals. Data at time 0 was omitted, since the cells were not fully settled. Data at time 7 and time 26 were also omitted, since it was concurrent with medium changes for each well plate, resulting in 36 time-points as a total.

Quantification of ALP activity

Quantitative ALP activity assays were performed as previously described [9]. After 18 days of culture, cell number was measured using a cell counting kit-8 (WST-8®; Dojindo Laboratories, Kumamoto, Japan), and ALP activities were measured with a p-nitrophenyl phosphate solution (Lab Assay ALP®; Wako Pure Chemical Industries, Ltd.). Briefly, for cell count, 100 µl of WST-8 was added to each well containing 1 mL of fresh medium, incubated for 1 hour, and absorbance was read at 450 nm. After WST-8 analysis, each well was washed twice with phosphate buffered saline (PBS) and 800 µL of p-nitrophenyl phosphate solution was added to each well. After 10 min of incubation at 37°C, the conversion to p-nitrophenol was stopped with 800 µl of 3N NaOH and the absorbance of p-nitrophenol was measured at 405 nm. Alkaline phosphatase-specific activity is expressed as p-nitrophenol absorbance (OD; 405 nm)/WST-8 absorbance (OD; 450 nm).

Calcium deposition quantification

After 25 days of culture, cells were fixed with 70% ethanol for 1 hour, washed, and stained for 10 min with 40 mM alizarin red S solution (pH: 4.2). After washing with PBS, plates were incubated with 10% cethylphridinium chloride for 15 min. Thereafter, supernatants were collected from each well and the absorption of each supernatant was measured at 405 nm to determine the amount of calcium deposition.

Cell image processing

All images (.bmp files) were processed by MetaMorph (Molecular device, CA, U.S.A) with the original combination of image-processing filter sets (Fig. 10–A). Briefly, the raw images were pre-processed by open-close filters and binarized by the optimized threshold. All image data was pre-processed using the same brightness threshold, which was optimized by 20 randomly picked image samples. This pre-processing step minimized error between the manually determined image cell number and the number of objects determined after pre-processing. After binarization, all individual objects in each image, consisting of cells and noise (non-cell objects), were measured by the integrated morphometric analysis function to measure morphological features (9 morphological features are: Breadth, Elliptical form factor, Fiber breadth, Fiber length, Hole area, Inner radius, Relative hole area, Shape factor, Total) (Fig. 10–B). The morphological features were carefully selected with the MetaMorph measurement function by logical selection. Features related to color and brightness were excluded first. Second, independent features were selected by hierarchical clustering and highly correlated features ($R>0.85$) were excluded. From the data consisting of object ID and its standardized 9 morphological features (average = 0, standard deviation = 1), the noise data (non-cell objects) was automatically cleansed by the original noise-reduction algorithm

prior to the analysis (patent pending). From the pre-processed data, average (AVE) and standard deviation (SD) from each of the 9 morphological features was calculated from each of the cell objects covering five view fields from the same well, and used as the 18 inputs (9 features with AVE and SD) for each sample to be used in further analysis (Fig. 10–C). The morphological features and cell number (AVE and SD for 19th and 20th feature) from each well were then tagged with the target signals, which are experimentally determined values, resulting in 54 samples (= 3 lots ×2 induction conditions ×3 passages ×3 wells) tagged with ALP values, and 54 samples tagged with calcium deposition values. This process links the "result" (biological measurement) with the "indication" (image-derived morphological feature), to derive a dataset for further modeling (Fig. 10–D).

Construction and evaluation of prediction model

Prediction of differentiation potential consists of two steps (Fig. 10–D): one is the construction of a prediction model, and the other is the evaluation of the constructed model. Using Ridge regression, two types of prediction models were constructed: (1) D14_ALP model, and (2) D21_Ca model. For the new patient scheme, prediction models were trained with 36 samples from 2 lots, and 18 samples from the remaining single lot were predicted. For the ongoing patient scheme, prediction models were trained with 42 samples from 2 lots of 3 passages plus the samples from new lot of 1 or 2 passages were used for training, and 12 samples from the remaining 1 lot were predicted (Fig. 5). The detailed modeling process is described in a previous report (See Section 3 in [18] for details of the Ridge regression method). The performance of each of the models and datasets were evaluated by the average accuracy resulting from leave-one-out cross validation.

For the evaluation of our proposed scheme, two evaluation indices are introduced in our work. One index is the correlation coefficient (R) of actual assay values and prediction values, which evaluates the prediction accuracy and its data coverage. The higher R increases, the more the model is capable of predicting "differentiation marker values" with small error rate. The other index of evaluation that we introduced is the average of absolute error. This value is calculated by obtaining absolute values of (experimentally determined value minus the predicted value). To compare these errors, we standardized these errors by dividing the variance of total experimentally determined values in one assay.

Supporting Information

Table S1 * Exp. determined rate is the abbreviation of the experimentally determined rate.
(XLS)

Table S2 * Exp. determined rate is the abbreviation of the experimentally determined rate.
(XLSX)

Acknowledgments

We are grateful to Mai Okada and Yurika Nonogaki for supporting the experiments and data storage. We also thank Wakana Yamamoto, Yoshihide Nagura, Kazuhiro Mukaiyama, Kenji Kojima, Hiroto Sasaki, and Asuka Miwa for establishing basal analysis protocol and algorithms for image analysis procedure.

Author Contributions

Conceived and designed the experiments: FM HK HA RK. Performed the experiments: FM. Analyzed the data: IT FM RK. Contributed reagents/materials/analysis tools: HS YK HH RK. Wrote the paper: FM IT HK HA RK.

References

1. Wu Y, Chen L, Scott PG, Tredget EE (2007) Mesenchymal stem cells enhance wound healing through differentiation and angiogenesis. Stem Cells 25: 2648–2659.
2. Chen L, Tredget EE, Wu PY, Wu Y (2008) Paracrine factors of mesenchymal stem cells recruit macrophages and endothelial lineage cells and enhance wound healing. PLoS ONE 3: e1886.
3. Barry FP, Murphy JM (2004) Mesenchymal stem cells: clinical applications and biological characterization. Int J Biochem Cell Biol 36: 568–584.
4. Hayashi O, Katsube Y, Hirose M, Ohgushi H, Ito H (2008) Comparison of osteogenic ability of rat mesenchymal stem cells from bone marrow, periosteum, and adipose tissue. Calcif Tissue Int 82: 238–247.
5. Mizuno D, Kagami H, Mizuno H, Mase J, Usami K, et al. (2008) Bone regeneration of dental implant dehiscence defects using a cultured periosteum membrane. Clin Oral Implants Res 19: 289–294.
6. Olivo C, Alblas J, Verweij V, van Zonneveld AJ, Dhert WJ, et al. (2008) In vivo bioluminescence imaging study to monitor ectopic bone formation by luciferase gene marked mesenchymal stem cells. J Orthop Res 26: 901–909.
7. Kagami H, Agata H, Tojo A (2011) Bone marrow stromal cells (bone marrow-derived multipotent mesenchymal stromal cells) for bone tissue engineering: Basic science to clinical translation. Int J Biochem Cell Biol. 43: 286–289.
8. Dennis JE, Esterly K, Awadallah A, Parrish CR, Poynter GM, et al. (2007) Clinical-scale expansion of a mixed population of bone-marrow-derived stem and progenitor cells for potential use in bone-tissue regeneration. Stem Cells 25: 2575–2582.
9. Agata H, Asahina I, Yamazaki Y, Uchida M, Shinohara Y, et al. (2007) Effective bone engineering with periosteum-derived cells. J Dent Res 86: 79–83.
10. Platt MO, Wilder CL, Wells A, Griffith LG, Lauffenburger DA. (2009) Multipathway kinase signatures of multipotent stromal cells are predictive for osteogenic differentiation: tissue-specific stem cells. Stem Cells. 27:2804–2814.
11. Kelly DJ, Jacobs CR (2010) The role of mechanical signals in regulating chondrogenesis and osteogenesis of mesenchymal stem cells. Birth Defects Res C Embryo Today. 90:75–85.
12. Kino-Oka M, Maeda Y, Sato Y, Maruyama N, Takezawa Y, et al. (2009) Morphological evaluation of chondrogenic potency in passaged cell populations. J Biosci Bioeng.107:544–551.
13. Carpenter AE, Jones TR, Lamprecht MR, Clarke C, Kang IH, et al. (2006) CellProfiler: image analysis software for identifying and quantifying cell phenotypes. Genome Biol. 7: R100.
14. Misselwitz B, Strittmatter G, Periaswamy B, Schlumberger MC, Rout S, et al. (2010) Enhanced CellClassifier: a multi-class classification tool for microscopy images. BMC Bioinformatics. 11: 30.
15. Harder N, Mora-Bermudez F, Godinez WJ, Wunsche A, Eils R, et al. (2009) Automatic analysis of dividing cells in live cell movies to detect mitotic delays and correlate phenotypes in time. Genome Res. 19: 2113–2124.
16. Jones TR, Carpenter AE, Lamprecht MR, Moffat J, Silver SJ, et al. (2009) Scoring diverse cellular morphologies in image-based screens with iterative feedback and machine learning. Proc. Natl. Acad. Sci. U. S. A. 106: 1826–1831.
17. Hoerl AE and Kennard R (1970) Ridge regression: biased estimation for nonorthogonal problems. Technometrics 12: 55–67.
18. Hastie T (2009) The Elements of Statistical Learning: Data Mining, Inference, and Prediction. Springer-Verlag. 43.

blood

2013 122: 4259-4263
doi:10.1182/blood-2012-08-451278 originally published online October 30, 2013

In vivo leukemogenic potential of an interleukin 7 receptor α chain mutant in hematopoietic stem and progenitor cells

Kazuaki Yokoyama, Nozomi Yokoyama, Kiyoko Izawa, Ai Kotani, Akira Harashima, Katsuto Hozumi and Arinobu Tojo

Blood (print ISSN 0006-4971, online ISSN 1528-0020), is published weekly by the American Society of Hematology, 2021 L St, NW, Suite 900, Washington DC 20036.

Brief Report

LYMPHOID NEOPLASIA

In vivo leukemogenic potential of an interleukin 7 receptor α chain mutant in hematopoietic stem and progenitor cells

Kazuaki Yokoyama,[1,2] Nozomi Yokoyama,[3] Kiyoko Izawa,[1] Ai Kotani,[4] Akira Harashima,[5] Katsuto Hozumi,[2] and Arinobu Tojo[1]

[1]Division of Molecular Therapy, Advanced Clinical Research Center, Institute of Medical Science, University of Tokyo, Tokyo, Japan; [3]Department of Laboratory Medicine, Research Hospital, Institute of Medical Science, University of Tokyo, Tokyo, Japan; [2]Department of Immunology and [4]Institute of Innovation Science and Technology, Tokai University School of Medicine, Kanagawa, Japan; and [5]Cell Biology Institute, Research Center, Hayashibara Biochemical Laboratories, Okayama, Japan

Key Points

- Gain-of function mutation of IL7Rα induces lymphoid leukemia as well as myeloproliferative disease.
- In vivo oncogenicity of mutant IL7Rα is influenced by the differentiation stage at which it occurs.

Somatic gain-of-function mutations in interleukin 7 receptor α chain (IL7Rα) have been described in pediatric T and B acute lymphoblastic leukemias (T/B-ALLs). Most of these mutations are in-frame insertions in the extracellular juxtamembrane-transmembrane region. By using a similar mutant, a heterozygous in-frame transmembrane insertional mutation (INS), we validated leukemogenic potential in murine hematopoietic stem/progenitor cells, using a syngeneic transplantation model. We found that ectopic expression of INS alone in hematopoietic stem/progenitor cells caused myeloproliferative disorders, whereas expression of INS in combination with a Notch1 mutant led to the development of much more aggressive T-ALL than with wild-type IL7Rα. Furthermore, forced expression of INS in common lymphoid progenitors led to the development of mature B-cell ALL/lymphoma. These results demonstrated that INS has significant in vivo leukemogenic activity and that the lineage of the resulting leukemia depends on the developmental stage in which INS occurs, and/or concurrent mutations. (*Blood*. 2013;122(26):4259-4263)

Introduction

Interleukin 7 (IL7) is essential for T-cell development and homeostasis.[1] Its cognate receptor (IL7R) forms a heterodimer composed of the α chain (IL7Rα) and common γ chain; binding of IL7 to IL7R triggers activation of Janus kinase (JAK)/signal transducer and activator of transcription signaling and the PI3K/v-akt murine thymoma viral oncogene homolog 1 (Akt) pathways.[1]

Accumulating evidence has demonstrated that dysregulation of the IL7 signaling axis may be implicated in lymphoid malignancies. For example, IL7 transgenic mice develop T- and B-cell lymphomas,[1] and human primary T-cell acute lymphoblastic leukemia (T-ALL) cells respond to IL7 in vitro[1] and in vivo.[2] Moreover, recent findings describing IL7Rα gain-of-function mutations in pediatric ALL and a T-ALL cell line have provided direct evidence that the IL7-IL7R axis plays a crucial role in the pathogenesis of human ALL.[3-6]

Although the gain-of-function properties of these mutants have been precisely studied in vitro,[3-5] their leukemogenic potential in vivo has not been well studied. One study reported that T-cell leukemogenesis was triggered by an IL7Rα mutant.[5] However, they used murine IL7-dependent D1 progenitor T-cell lines derived from p53-knockout mice,[7] which spontaneously develop T-cell lymphoma,[8,9] and this specific animal model may not be generally applicable.

To extend these observations, we demonstrate the in vivo leukemogenic potential of such a mutant when expressed in primary hematopoietic stem and progenitor cells by using a IL7Rα mutant, which was previously identified in a T-ALL cell line.[6]

Methods

Mice

Six- to 12-week-old Balb/c mice were used for all experiments. Lineage depletion of bone marrow (BM) or embryonic day 14.5 (E14.5) fetal liver was performed by the EasySep Mouse Hematopoietic/Progenitor Cell Enrichment Kit (StemCell Technologies). Via tail vein injection, 1×10^6 Lineage$^-$ BM/fetal liver cells (lin$^-$ cells), pro-B, or Thy1$^+$T cell progenitors were injected into lethally (8 Gy) or sublethally (4 Gy) irradiated recipients. Mice were maintained in accordance with institutional animal care guidelines (Institute of Medical Science, University of Tokyo). Detailed methods are provided in the supplemental Methods.

Submitted August 20, 2012; accepted October 10, 2013. Prepublished online as *Blood* First Edition paper, October 30, 2013; DOI 10.1182/blood-2012-08-451278.

K.Y. and N.Y. contributed equally to this study.

The online version of this article contains a data supplement.

There is an Inside *Blood* commentary on this article in this issue.

The publication costs of this article were defrayed in part by page charge payment. Therefore, and solely to indicate this fact, this article is hereby marked "advertisement" in accordance with 18 USC section 1734.

Biol Blood Marrow Transplant 20 (2014) 577–592

Brief Articles

Effect of ABO Blood Group Incompatibility on the Outcome of Single-Unit Cord Blood Transplantation after Myeloablative Conditioning

Takaaki Konuma [1,*], Seiko Kato [1], Jun Ooi [2], Maki Oiwa-Monna [1], Yasuhiro Ebihara [1], Shinji Mochizuki [1], Koichiro Yuji [1], Nobuhiro Ohno [1], Toyotaka Kawamata [1], Norihide Jo [1], Kazuaki Yokoyama [1], Kaoru Uchimaru [1], Arinobu Tojo [1], Satoshi Takahashi [1]

[1] *Department of Hematology/Oncology, The Institute of Medical Science, The University of Tokyo, Tokyo, Japan*
[2] *Department of Hematology/Oncology, Teikyo University School of Medicine, Tokyo, Japan*

Article history:
Received 1 November 2013
Accepted 18 December 2013

Key Words:
Cord blood transplantation
ABO incompatibility
Graft-versus-host disease
Myeloablative conditioning

A B S T R A C T

ABO blood group incompatibility between donor and recipient has been associated with poor transplant outcomes in allogeneic hematopoietic stem cell transplantation. However, its effect on the outcome of cord blood transplantation (CBT) has yet to be clarified. We retrospectively analyzed 191 adult patients who received single-unit CBT after myeloablative conditioning for malignant disease in our institute. Major mismatch showed a significantly lower incidence of platelet engraftment compared with ABO match as a reference (hazard ratio, .57; $P = .01$). Nevertheless, there was no increase in graft-versus-host disease, transplant-related mortality, and overall mortality after ABO-incompatible CBT. These data suggested that donor–recipient ABO incompatibility does not have a significant impact on outcome after myeloablative CBT for hematological malignancies.

INTRODUCTION

In contrast to solid organ transplantation, ABO blood group incompatibility between donor and recipient is reportedly a more common situation after allogeneic hematopoietic stem cell transplantation (allo-HSCT). It is well known that ABO incompatibility of allo-HSCT can cause an increased risk of delayed erythroid reconstitution, pure red cell aplasia, and acute and delayed hemolysis [1,2]. However, the association between ABO incompatibility and transplantation outcomes, such as neutrophil and platelet recovery, graft-versus-host disease (GVHD), and survival, is controversial [1,2]. Moreover, most of these studies analyzed patients receiving allo-HSCT using bone marrow or mobilized peripheral blood as a stem cell source from related and unrelated donors [1-5].

Cord blood transplantation (CBT) from an unrelated donor is increasingly used as an alternative transplant method for adult patients without HLA-compatible related or unrelated donors. Although most patients receive an HLA-mismatched cord blood unit, the lower risk of GVHD without compromising graft-versus-leukemia effects is one of the most attractive advantages of CBT. We previously reported that ABO incompatibility influenced platelet engraftment and transfusion requirement of RBCs and platelets in CBT [6]. However, the effects of ABO incompatibility on GVHD and survival after myeloablative CBT are limited. In the present study, we analyzed the neutrophil and platelet recovery, GVHD, transplant-related mortality (TRM), relapse, and survival in myeloablative CBT in adult patients with malignant disease in our institute.

METHODS

This retrospective study included data from 191 adult patients who underwent unrelated first allogeneic transplantation using single-unit CBT at our institute between August 1998 and February 2013. Donor–recipient ABO compatibility was categorized as follows: ABO match in 55 patients, major mismatch in 47, minor mismatch in 58, and bidirectional mismatch in 31. All patients received 12 Gy total body irradiation (TBI)-based myeloablative conditioning regimens and cyclosporine with or without short-term methotrexate as a GVHD prophylaxis, and cord blood units were selected as reported previously [7,8]. The institutional review board of the Institute of Medical Science, The University of Tokyo approved this study. This study was conducted in accordance with the Declaration of Helsinki.

The primary study endpoint was overall survival (OS), defined as the time from the date of transplantation to the date of death or last contact. Secondary endpoints were relapse, TRM, GVHD, and neutrophil and platelet recovery. Relapse was defined by morphologic evidence of disease in peripheral blood, bone marrow, or extramedullary sites. TRM was defined as death during a remission. Both acute GVHD (aGVHD) and chronic GVHD (cGVHD) were graded according to previously published criteria [9,10]. The incidence of aGVHD was evaluated in all engrafted patients, whereas the incidence of cGVHD was evaluated in engrafted patients surviving more than 100 days. Neutrophil engraftment was defined as being achieved on the first of 3 consecutive days during which the absolute neutrophil count was at least 0.5×10^9/L. Platelet engraftment was defined as being achieved on the first of 3 days when the platelet count was higher than 50×10^9/L without transfusion support.

Baseline patient and transplant characteristics were compared using the chi-square test for categorical variables and the Kruskal-Wallis test for continuous variables. The probability of OS was estimated according to the

Financial disclosure: See Acknowledgments on page 580.

* Correspondence and reprint requests: Takaaki Konuma, Department of Hematology/Oncology, The Institute of Medical Science, The University of Tokyo, 4-6-1, Shirokanedai, Minato-ku, Tokyo 108-8639, Japan.
E-mail address: tkonuma@ims.u-tokyo.ac.jp (T. Konuma).

1083-8791/$ – see front matter © 2014 American Society for Blood and Marrow Transplantation.
http://dx.doi.org/10.1016/j.bbmt.2013.12.563